


Hall-effect sensors based on AlGa_N/Ga_N heterojunctions on Si substrates for a wide temperature range

Sagnik Kumar¹  | R. Muralidharan² | G. Narayanan¹

¹Department of Electrical Engineering, Indian Institute of Science, Bengaluru, India

²Centre for Nano Science and Engineering, Indian Institute of Science, Bengaluru, India

Correspondence

Sagnik Kumar, Department of Electrical Engineering, Indian Institute of Science, Bengaluru, India.

Email: sagnikkumar@alum.iisc.ac.in

Funding information

Ministry of Electronics and Information technology, Grant/Award Number: 25(6)/2019-ESDA

Abstract

The authors report experimental investigations on Hall sensors based on AlGa_N/Ga_N heterojunctions grown on silicon 111 (Si 111) substrates. Realisation of two-dimensional electron gas-based Hall sensors on Si substrates can have the advantages of low cost and integrability with complementary metal-oxide semiconductor circuits. Design and fabrication of such Hall sensors and their characterisation over a wide temperature range of 75 to 500 K are reported. The authors experimentally investigate the temperature dependence of the transresistances, sheet resistance and current-related sensitivity (or gain) of such Hall sensors. The current-related sensitivity is shown to be reasonably constant over the complete temperature range and certain inevitable variations in current-related sensitivity can easily be compensated. The temperature dependence of the transresistance can be used for such compensation. The variation of the geometrical correction factor of the Hall sensor with the applied magnetic field strength and the operating temperature is also studied. The authors also demonstrate the possibility of realising Hall sensors with a high geometrical correction factor (≈ 0.97), which is practically insensitive to variations in temperature ($\approx 2\%$ from 75 to 500 K) and applied magnetic field, for applications such as in electromechanical devices.

1 | INTRODUCTION

Magnetic field sensing is being used widely in many scientific and industrial domains for direct measurement of fields, indirect estimation of physical variables such as position or velocity, detection of material defects etc. A few of the diverse applications include geophysical exploration [1], deep space and planetary magnetometry [2], target detection [3, 4], medical imaging [5], spectroscopic investigation of chemical compounds [6], non-destructive testing of ferromagnetic and metallic objects including identification of cracks [7], read-heads in disk drives [8], proximity sensing [9], rotor position sensing and speed sensing in motors [10], non-contact measurement of current through a conductor [11] and transformer in-rush current in power systems [12], fake currency detection [13] and navigation [14].

Depending on the underlying principle of the field measurement, magnetic sensors can be mainly classified into the search-coil magnetometer, flux-gate magnetometer, giant magnetoresistance sensor, Hall-effect sensor and

superconducting quantum interface device [15]. Each technique has its advantages in a certain sensitivity range, though the latter is also influenced by the readout electronics. The suitability of a sensor for a particular application depends on the size, cost and performance metrics such as resolution, bandwidth and power consumption.

Hall sensor have proved to be an attractive solution for sensing requirements from a few hundred teslas down to a nano tesla [16, 17]. It is utilised extensively in electric machines for position sensing, torque measurement [18], measurement of stray magnetic field to determine efficiency [19], and implementation of field oriented control [20]. In addition, they are used in monitoring of magnetic fields at the surface of the samples such as in scanning Hall probe microscopy [21] and magnetic force microscopy [22]. Recently, there has been a demand for the stable Hall sensor operation at extreme temperatures [23, 24] and also in harsh radiation environments as encountered in space exploration, determination of Curie temperatures of ferromagnetic materials [25], magnetic diagnosis of thermonuclear reactors

This is an open access article under the terms of the Creative Commons Attribution License, which permits use, distribution and reproduction in any medium, provided the original work is properly cited.

© 2021 The Authors. *IET Circuits, Devices & Systems* published by John Wiley & Sons Ltd on behalf of The Institution of Engineering and Technology.

[26] and current sensing in electric vehicles [27]. Emergence of new promising materials and advances in processing technologies continue to propel research on Hall sensors [28–33].

An essential requirement of Hall sensing is to establish a thin conducting sheet which is perpendicular to the direction of the magnetic field to be measured. The popular complementary metal-oxide semiconductor (CMOS) Hall plate (see Figure 1) utilises the inversion layer under its gate as the thin conducting sheet [34]. Alternatively, thin films of group III–V compounds (not illustrated) such as InAs or InSb could be employed to realise such conducting sheets [35, 36]. The bias current in the conducting sheet flows through one pair of diagonal terminals (e.g. source S and drain D in Figure 1); the Hall voltage is sensed across the other diagonal pair (H+ and H– in Figure 1). A CMOS Hall plate can be easily integrated with the Si-based on-chip signal conditioning and read-out electronic circuits. However, its performance degrades above 423 K [37]. Thin film Hall sensors based on group III–V compounds offer much higher sensitivity (i.e. gain) than CMOS Hall plate, but their operating temperature range is even more limited [38] owing to lower band gap of III–V compounds.

The two-dimensional electron gas (2DEG) formed at the heterostructural junctions of III–V ternary compounds [33, 39, 40] is yet another option in this regard which could be viable and attractive. Some of the widely reported III–V quantum well structures include those of AlGaAs/InGaAs [33, 39], InAsSb/InAlSb [41] and AlGaN/GaN [25]. One such structure is illustrated in Figure 2. InAsSb/InAlSb-based Hall sensors provide much higher sensitivity than their AlGaAs/InGaAs and AlGaN/GaN counterparts. However, the sensitivity of such sensor degrades rapidly above room temperature [42]. The stability of the AlGaAs/GaAs Hall sensors degrades above 473 K [42]. Though AlGaN/GaN-based 2DEG sensors have been reported to have the lowest sensitivity, they have much superior temperature stability and can remain operational at least up to 673 K [25, 40, 42].

Existing commercial Hall sensors are mostly Si-based [43, 44]; a few of them are thin-film based [45–47]. Though it is widely acknowledged in the literature that the 2DEG Hall sensors based on AlGaN/GaN heterostructures can provide stable sensitivity over a wide range of temperature [25, 32, 42, 48–51], and very few commercial sensors are 2DEG based [52, 53]. These known commercial Hall sensors are also not based on AlGaN/GaN heterostructures. This paper evaluates AlGaN/GaN heterostructure based Hall sensor for possible

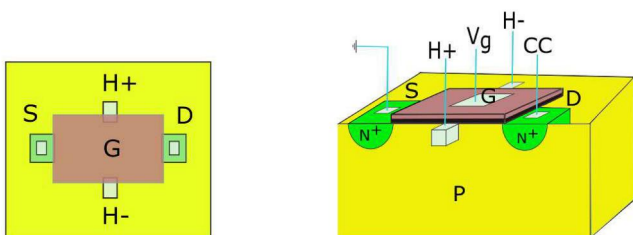


FIGURE 1 CMOS Hall plate [34]

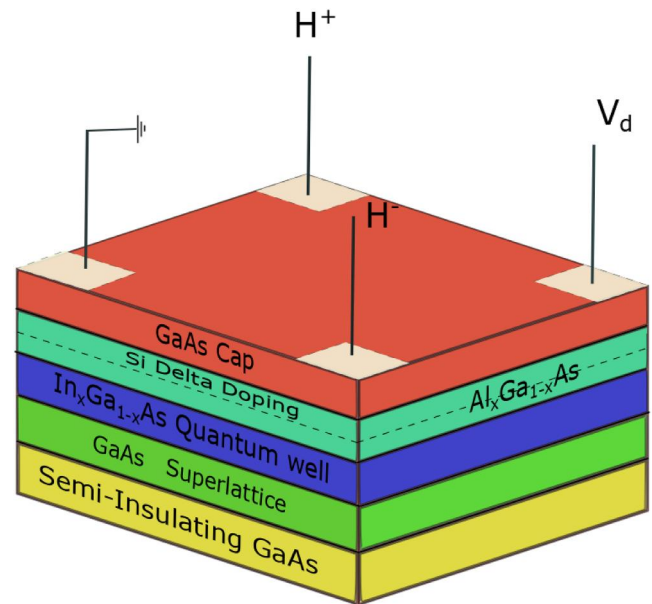


FIGURE 2 AlGaAs/InGaAs/GaAs pseudomorphic heterostructure featuring 2DEG in InGaAs quantum well [33]

commercial exploitation by investigating its performance over wide operating range, stability and extent of variation of performance characteristics against temperature variation, possibility of compensating for the temperature dependence of performance, and estimation of sample temperature through electrical terminal measurements. This article also considers such choice of geometry and substrate which are advantageous from the perspectives of ease of production, cost of production, and integrability of the sensor with other peripheral electronic circuitry.

The choice of substrate for the epitaxial growth of the AlGaN/GaN layers is an important consideration for commercial deployment. SiC, sapphire and Si are the popular choice of substrates. Despite the high thermal conductivity of SiC [54, 55] and it having close lattice match to that of GaN [56], the production of large defect-free SiC wafers is a challenge [56]. On the other hand, despite the large lattice mismatch between sapphire and GaN [56], growth of defect-free epitaxial GaN layers on sapphire has become possible, thanks to the research efforts over decades [56, 57]. Many of the reported AlGaN/GaN Hall sensors are grown on sapphire substrates, including some recent application [32]. Silicon (Si) substrates offer the much needed integrability of the Hall sensing element with CMOS on-chip signal conditioning circuits [28] in applications where the operating temperature range allows the use of CMOS technology. Numerous methods have been proposed in this regard [58, 59]. One such method involves fabricating the signal conditioning circuitry on Si wafers using the CMOS technology followed by the epitaxial growth of the AlGaN/GaN heterojunctions using molecular beam epitaxy in ‘windows’ defined directly on the Si substrate [59]. Large area defect-free Si substrates can be easily realised and cost of substrate production is quite low [29]. Thermal

conductivity of Si is also much higher than that of sapphire. However traditionally there have been growth-related issues of epitaxial GaN layers on Si substrates due to the large lattice mismatch [56]. With the growth related issues having been addressed adequately in recent times [28, 30], AlGa_N/GaN-based Hall sensor on Si substrate appears to be an attractive option presently.

While the current-related sensitivity of Hall sensors based on AlGa_N/GaN heterojunctions has been reported extensively [25, 32, 40, 42, 48–51], studies of such Hall sensors on Si substrates are rather limited [31, 40, 50, 51]. The sensitivity is mostly reported at a fixed value of the magnetic field [40, 51] or over a range of low values of the field [25, 32, 42, 48–50]. Experimental study on the variation in sensitivity is necessary not only over a wide range of temperatures, but over a wide range of magnetic field as well. Geometry of the sensor is another important factor that influences sensor performance and cost. The geometry introduces an additional factor termed as the geometrical correction factor in the sensitivity or gain of the sensor. A recent work has reported geometrical correction factor of a 2DEG-based Hall sensor at room temperature [31]. However, the variation of this factor with temperature as well as field needs to be studied.

This article reports design and fabrication of Hall sensors based on AlGa_N/GaN heterostructures grown on Si substrates. The current related sensitivity of the sensor is studied experimentally over a wide range of temperature from 75 to 500 K under external field strengths up to 2 T. The trans-resistances and sheet resistances are studied experimentally over the same temperature range. Possible methods of compensation, based on terminal measurements of the Hall sensor, for the inevitable variation in sensitivity with temperature are suggested. The variations in the geometrical correction factor with the operating temperature and the applied field are studied over the complete range of interest.

2 | HALL COEFFICIENT AND GEOMETRICAL CORRECTION FACTOR

Analytical expressions related to the performance of Hall sensors are reviewed. Hall coefficient R_H and geometrical correction factor G_H of a Hall sensor are defined and discussed.

2.1 | Ideal sensor analysis

The ideal Hall voltage generated across the finite width w of an infinitely long ($l \gg w$) conductor, carrying current I in the longitudinal direction, and subjected to a normal magnetic field B is given by [60]:

$$V_{H\infty} = \frac{R_{H,id}IB}{t} \quad (1)$$

Thus, V_H is directly proportional to bias current I and field magnitude B , and is inversely proportional to the thickness of the conductor. The constant of proportionality, namely, the ideal Hall coefficient, $R_{H,id}$, is given by:

$$R_{H,id} = \frac{1}{qn} \quad (2)$$

where, q is charge on an electron and n is carrier concentration. The current related sensitivity, S_I of the sensor is the ratio of $V_{H\infty}$ to the product IB as shown [60]:

$$S_I = \frac{V_{H\infty}}{IB} = \frac{1}{qnt} = \frac{1}{qn_s} \quad (3)$$

where n_s is the sheet carrier density. The sheet resistance R_s is the ratio of resistivity ρ of the conducting layer (here, the 2DEG) to its thickness t :

$$R_s = \frac{\rho}{t} \quad (4)$$

Under ideal condition, the mobility μ of the carriers can be obtained using n_s and R_s as shown in the following equation:

$$\mu = \frac{1}{qn_s R_s} \quad (5)$$

2.2 | Actual Hall coefficient

The idealised analysis in (1)–(5) assumes that the carriers move with the same drift velocity in the presence of a constant electric field applied to the sample. In addition, ρ and n_s are assumed to be uniform. However, in a practical finite dimensional Hall plate, the carriers experience collisions. The carrier transport is also influenced by energy distribution of carriers.

Considering the above factors, an accurate analysis of the galvanometric transport of carriers using the Boltzmann kinetic equation yields the following expression for the practical Hall coefficient R_H [60]:

$$R_H = \frac{1}{em^*} \frac{1}{1 + \left(\frac{e}{m^*} \frac{K_2}{K_1}\right)^2} \frac{K_2}{B^2 K_1} \quad (6)$$

where m^* is the effective mass of carriers participating in conduction; K_1 and K_2 are the kinetic coefficients given by the following integrals [60]:

$$K_1 = \frac{2}{3m^*} \int_0^\infty \frac{E\tau(E)}{1 + \mu^2(E)B^2} g_c(E) \left(-\frac{\partial F_0}{\partial E}\right) dE \quad (7)$$

$$K_2 = \frac{2}{3m^*} \int_0^\infty \frac{E\tau^2(E)}{1 + \mu^2(E)B^2} g_c(E) \left(-\frac{\partial F_o}{\partial E} \right) dE \quad (8)$$

Here τ is the relaxation time of carriers; $g_c(E)$ is the density of states in the conduction band; E is the energy of the carriers relative to the bottom of the conduction band (which is equivalent to their kinetic energy); and $F_o(E)$ is the probabilistic, energy-dependent distribution function of carriers at equilibrium.

As seen from (6) to (8), the practical Hall coefficient exhibits certain dependence on B , rendering Hall voltage to be a non-linear function of B . However, a good Hall sensor should make sure that the non-linearity is small and negligible. In case of non-degenerate carriers, the non-linearity is only negligible at very low magnetic inductions and the Equation (10) can be simplified to [60]:

$$R_{H,nd} = \frac{r_b}{qn} \quad (9)$$

where $R_{H,nd}$ denotes the Hall coefficient for non-degenerate semiconducting Hall plate and r_b is the Hall scattering factor given by [60]:

$$r_b = \frac{\langle \tau^2 \rangle}{\langle \tau \rangle^2} \quad (10)$$

$\langle \tau^s \rangle$ is the energy-weighted average relaxation time to the power s . Thus, the Hall coefficient for non-degenerate semiconductors $R_{H,nd}$ differs from $R_{H,id}$ by a factor of r_b .

For strongly degenerate semiconductors, the partial derivative of the distribution function approximately satisfies the following condition [60]:

$$\frac{\partial F_o}{\partial E} \approx \delta(E - E_F) \quad (11)$$

where E_F is the Fermi energy. This essentially implies that all carriers in a strongly degenerate semiconductor are present in a very small energy band around the Fermi energy. Under this approximation, r_b simplifies to 1 and R_H in (6) simplifies to $R_{H,id}$ in (2).

2.3 | Geometrical correction factor

As previously mentioned, Equation (1) holds true for an infinitely long plate-like ($l \gg w$) sensing element which is practically infeasible. The effect of the dimensions being finite shows up as a reduction in the Hall voltage, which can be captured by multiplying a fraction termed as geometrical correction factor G_H to the ideal Hall voltage expression as shown [60]:

$$V_H = G_H V_{H\infty} \quad (12)$$

The geometrical correction factor has been obtained by conformal mapping techniques for many different geometries such as square, Greek-cross, clover-leaf and octagon [61]. For a square-shaped geometry, G_H is shown to depend on the Hall angle (θ_H) and the ratio of the sum of the lengths of the ohmic contacts to the perimeter of the square (λ). If the contacts are sufficiently small and at the corners ($\lambda < 0.59$), an approximate formula has been derived in [61] which is reproduced as shown here:

$$G_H(\lambda, \theta_H) = 1 - 0.696\lambda^2 \left(1 - \frac{\theta_H^2}{3} \right) \quad (13)$$

$$\theta_H = \tan^{-1}(\mu B) \quad (14)$$

Apart from λ , G_H depends on the Hall angle θ_H which, in turn, depends on the product of μ and B .

3 | DEVICE FABRICATION

The steps in fabrication of Hall sensor are detailed in this section.

3.1 | Device geometry

Small Hall sensors are used to measure B at a point. However, in applications such as electric machines where the average B over a certain area is required, Hall elements need to have larger sensing areas. Here, large Hall sensors of 1.25 cm square-shaped geometry are fabricated and characterised. Square-shape, apart from being the simplest geometry, also ensures economical use of wafer. The square shape of the active area and the relative dimensions of the ohmic contacts impact G_H as mentioned earlier. Small ohmic contacts result in a low value of λ , which makes G_H high [60, 61]. However a recent study has shown that making the contacts too small can contribute a significant noise to the developed Hall voltage, thus, degrading the signal-to-noise ratio (SNR) of the Hall-effect device [62]. Further, the ohmic contacts are chosen to be squares of 0.125 cm side which results in $\lambda = 0.2$.

3.2 | Dicing and surface preparation

The GaN-on-Si wafers (of the structure illustrated in Figure 3 (a)), are first diced into 1.25 cm square samples using an automated dicing equipment (Disco DAD321 Wafer Dicer [63]), capable of dicing Si and pyrex glass wafers, with a blade width of 0.2 mm. The diced samples are dipped in an aqueous solution of HCl (i.e. one part of MOS grade HCl mixed with

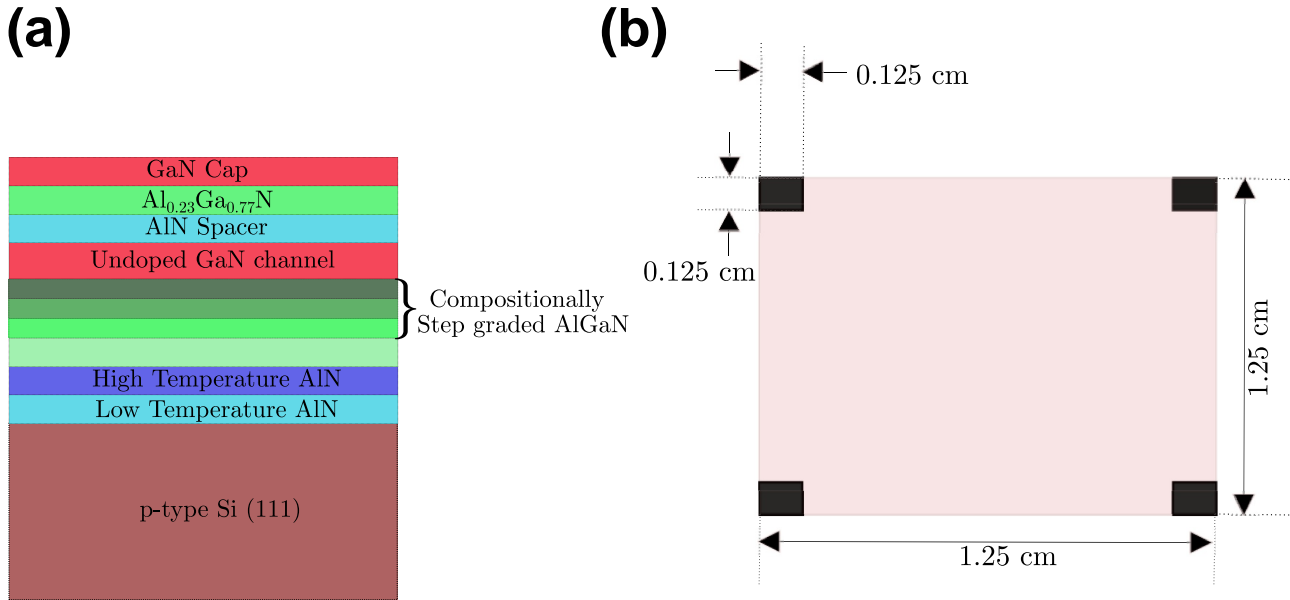


FIGURE 3 (a) Cross-sectional diagram of the layered Hall structure and (b) schematic of the fabricated Hall-sensing element

four parts of deionised H_2O) for 30 s to etch away the native oxide layer on GaN sample. This prepares the sample surface for metal deposition subsequently.

3.3 | Shadow masking/lithography

Note that only the areas of the wafer surface where metal has to be deposited for ohmic contacts need to be exposed; the other regions should be masked. This can be achieved by a lithography step where a photoresist is coated on the wafer surface and patterns are inscribed on the resist by a mask-writer equipment [64]. Since, the four contacts needed at the corners are relatively larger in the present case, a comparatively simpler alternative of shadow masking is adopted. Kapton tapes are used to cover the wafer surface and side-walls, leaving only the corners exposed. The samples are then loaded into the evaporation chamber of the e-beam evaporator (TECPORT) [65].

3.4 | Metal deposition

The metal to be deposited on the sample is heated above its melting point by means of electron beam inside an evacuated chamber. The electron beam is produced by thermionic emission from a tungsten filament, and is directed on the metal by a suitable magnetic field to melt the metal. The metal vapour is allowed to gradually condense and deposit on the sample until the metal thickness grows to the desired extent [66].

The evaporation chamber is evacuated to a very low pressure of the order of 10^{-6} Torr, a process which takes about 2–3 h, in the given e-beam evaporator. To initiate and sustain a stable thermionic emission, the current through a tungsten

TABLE 1 Details of the metal stack in each sample

Sample	Metal layers and their thicknesses
Sample 1	Ti (20 nm), Al (120 nm)
Sample 2	Ti (25 nm), Al(150 nm), Ni (30 nm), Au (100 nm)

filament is gradually ramped up over a few minutes (called the rise stage); the current is then maintained at the same value over a few more minutes (otherwise called the soak stage) to stabilise the temperature of the molten metal. The filament current is increased to its desired value over 2 or 3 such cycles, consisting of rise and soak stages. During this process the volatile impurities are removed. After the maximum emission current is reached, the sample is exposed to the vapours [65].

The sample holders are rotated in a planetary fashion in order to achieve good uniformity in the deposited metal thickness over the surface of the sample. A quartz-crystal oscillator is located in close proximity to the sample holders and monitors the thickness of the metal stack deposited. Vapours of metal deposited on the quartz crystal increases its mass and reduces its natural frequency. Through suitable mathematical transformations, the change in frequency is converted to a change in thickness of the metal deposited on the sample [65].

Two samples are prepared here. In sample 1, a 20 nm layer of titanium (Ti) is deposited first; this is followed by deposition of an aluminium layer (Al) which is 120 nm thick, as indicated in Table 1. Thus, sample 1 has a two-layer metal stack. This is also the minimum requirement for making ohmic contacts in an AlGaIn/GaN sample. On sample 2, 30 nm of nickel (Ni) layer followed by 100 nm of gold (Au), is also deposited on top of a Ti/Al metal stack. The four layer metal stack of Ti/Al/Ni/Au stack is more commonly used for good ohmic contacts to the 2DEG in AlGaIn/GaN heterojunctions [25, 32, 42, 50].

3.5 | Rapid thermal annealing

Post deposition, each sample is subjected to annealing in an ANNEALSYS rapid thermal processing furnace [67] in an N_2 ambient at 1123 K for 45 s. Annealing results in the formation of TiN which penetrates the AlGaIn layer and makes a direct link between the ohmic contact at the top and the 2DEG aluminium controls the rate of displacement reaction between Ti and GaN, and also forms intermetallic compounds with Ti to lower the contact resistance. Aluminium has the propensity to develop a layer of native oxide on exposure to air rendering the contacts unreliable for device applications. To prevent aluminium from oxidizing, Ni/Au overlayer is used in sample 2. Ni prevents the out-diffusion of Al and the formation of Al/Au alloy which exhibit lower conductivity and can potentially degrade the quality of ohmic contacts to the 2DEG. The sample can now be taken for characterisation.

4 | CHARACTERISATION SETUP

The two samples are characterised at different temperatures using a cryogenic probe station [68]. This probe station is capable of 4-probe DC, radio frequency and microwave electrical measurements. The temperature of the sample can be maintained at a given temperature, which can range anywhere between liquid helium temperature and 500 K. Further, normal magnetic field of specified strength can be applied on the sample using a superconducting cryogenic magnet. For generating a magnetic field, the magnet-stage needs to be cooled down to a temperature of 5 K using a two-stage closed cycle refrigeration (CCR) process where liquid helium is used as the working fluid.

The sample-stage temperature is controlled at the desired value through a combination of thermal connections, cooling effect of the CCR stages, and heating effect of a resistive heater. There is a radiation shield present which is meant to prevent loss of heat from the CCR stages, the magnet-stage and the sample-stage. This shield is maintained at a temperature of around 50 K.

When the desired sample-stage temperature is lower than 35 K, the sample-stage is thermally connected to the magnet stage. If the set temperature is between 35 and 100 K, then the sample-stage is connected to the radiation shield. If the sample-stage temperature is between 100 and 500 K, then it has to be left thermally open. The temperature controller maintains the sample temperature precisely at the set point by employing requisite amount of resistive heating against the cooling effect of the CCR stage.

A set of probe tips contacts the pads in the sample for establishing electrical connections (as shown in Figure 5). Desired current can be injected by a semiconductor device analyser through a pair of probe tips into the sample. The voltage across the other pair of contacts of the sample can be measured through another pair of probe tips.

The probe tips are made of tungsten, which is non-magnetic and inert. Hence the probe tips do not influence the magnetic field applied, and are less prone to oxidation despite high

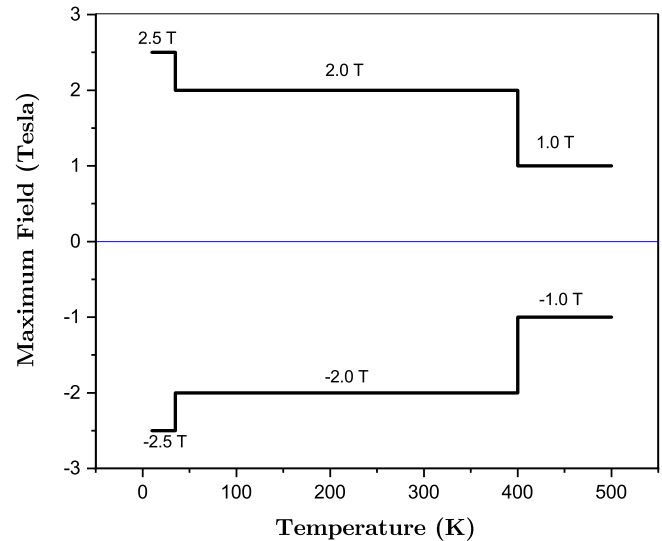


FIGURE 4 Graph showing the maximum field that can be generated with respect to the sample stage temperature

operating temperatures. Each probe tip is replaceable, if worn out with usage, to ensure good electrical contact.

The probe-arm assembly allows the probe tips to be translated in the x, y and z directions for probing the sample at the required points. Separate micrometre dials guide the movement of each probe arm along the three directions. The probes are thermally anchored on the radiation shield, and hence, are cooled to 50 K. The diameter of the probe tips used for the characterisation is 12.5 μm . This is very small compared to the dimensions of the sample. Hence, it can be safely assumed that the sample temperature is unaffected by the electrical connections made by the probes.

Though the magnet-stage is reasonably well-shielded, certain moderate increase in its temperature is inevitable when the sample-stage temperature is quite high. Hence the maximum field strength that can be generated by the cryogenic magnet is reduced from 2 to 1 T when the sample temperature is above 400 K. The limitations on the maximum field strength are illustrated in Figure 4.

The magnetic field strength is measured by sensing the current through the magnet coil and multiplying it with a field constant. The field constant is calibrated and set by the manufacturer as stated in the operating manual of the probe station [68]. Each magnet has a unique value of the field constant which can range from 0.071 to 0.075 Tesla/A [68].

During Hall measurements, the required field strength is adjusted using the magnet power supply. It ramps up/down the current in the superconducting magnet at a constant rate of 0.08 A/s until the field set point is reached. The time taken for a 0.25 T change in field is approximately 5 s.

As mentioned earlier, the sample-stage is maintained at the set point by a dynamic equilibrium between the resistive heating and cooling effect of the CCR stages. To increase the temperature, resistive heating is increased by the temperature controller. An increase of 25 K takes 5 min. During cooling of

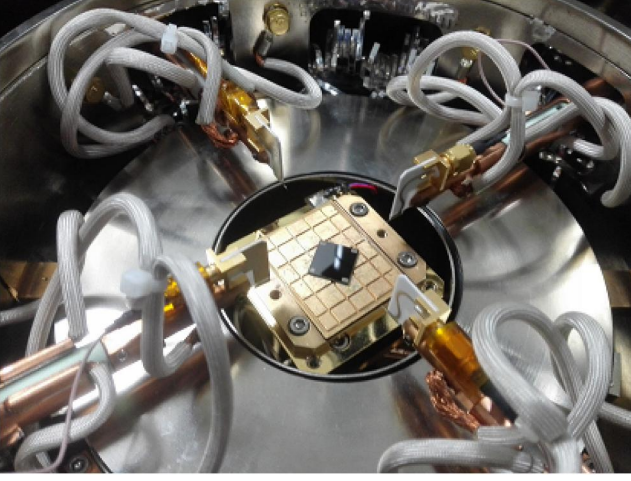


FIGURE 5 Sample-stage and probing arms of the cryogenic probe station

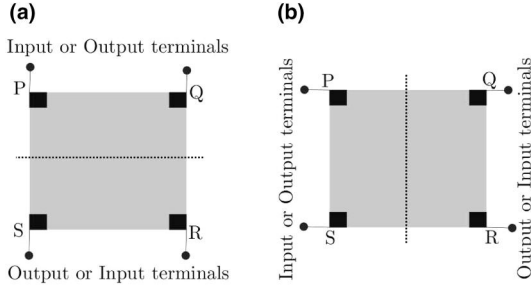


FIGURE 6 Representation of the Hall sensing element as a two port network (a) for determining transresistance R_1 and (b) for determining transresistance R_2

the sample stage, the heater power is reduced to near zero. A decrease of 25 K takes approximately 25 min.

5 | MEASURED SHEET RESISTANCE

The sheet resistance R_S of the two samples are measured over a temperature range of 75 to 500 K using the cryogenic probe station.

5.1 | Transresistances and sheet resistance

A Hall element is a 4-terminal device, which can be viewed as a two-port network with two adjoining terminals as the input port and the other two as the output port [69]. Terminals P and Q can be considered as the input port, while R and S can be regarded as the output port, or vice-versa, as shown by Figure 6(a). The transresistance of this two-port network is designated as R_1 . Alternatively, the terminals P and S can be paired as one port, while Q and R can be paired up as the other port, as illustrated in Figure 6(b). The transresistance of such a two-port network is denoted by R_2 . If the ohmic contacts are point-sized and are located exactly at the periphery of the

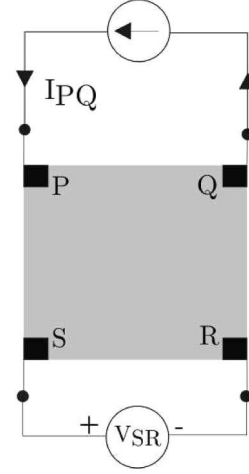


FIGURE 7 Measurement of transresistance, R_{1a} , through trial A

TABLE 2 Determination of R_1 to evaluate sheet resistance at $T = 300$ K

R_{1a}	R_{1b}	R_{1c}	R_{1d}	R_1
$\frac{V_{SR}}{I_{PQ}}$	$\frac{V_{RS}}{I_{QP}}$	$\frac{V_{PQ}}{I_{SR}}$	$\frac{V_{QP}}{I_{RS}}$	$\frac{R_{1a}+R_{1b}+R_{1c}+R_{1d}}{4}$
67.72 Ω	65.78 Ω	65.80 Ω	67.68 Ω	66.74 Ω

sample, the transresistances R_1 and R_2 are related to the sheet resistance by the following expression [70]:

$$e^{-\frac{\pi R_1}{R_S}} + e^{-\frac{\pi R_2}{R_S}} = 1 \quad (15)$$

The sheet resistance at a given temperature is determined using measured R_1 and R_2 at the same temperature using Equation (15). Since, the ohmic contacts fabricated in this work are not exactly point-like and have finite dimensions, so small errors are expected in the obtained values of R_S . A more accurate derivation of the sheet resistance from the measured voltages and currents in the Van Der Pauw setup as shown in Figure 7 can be found in [71].

5.2 | Measurement of transresistances R_1 and R_2

Trial A of the measurement of transresistance R_1 of the two-port network in Figure 6(a) involves injecting the current I_{PQ} into terminal P and out of terminal Q, and measuring the voltage V_{SR} between S and R; the ratio of V_{SR} to I_{PQ} gives the resistance R_{1a} (see Table 2). Similarly, R_{1b} is measured in trial B by reversing the direction of the current injection (i.e. I_{QP} instead of I_{PQ}), and measuring V_{RS} instead of V_{SR} , and obtaining the ratio V_{RS} to I_{QP} .

Similarly, transresistance values R_{1c} and R_{1d} are obtained in trials C and D, considering R and S to be the current injection terminals, and measuring the voltage across P and Q with appropriate polarity, as shown in Table 3. The average of R_{1a} , R_{1b} , R_{1c} and R_{1d} is taken as transresistance R_1 .

TABLE 3 Determination of R_2 to evaluate sheet resistance at $T = 300$ K

R_{2a}	R_{2b}	R_{2c}	R_{2d}	R_2
$\frac{V_{QR}}{I_{PS}}$	$\frac{V_{RQ}}{I_{SP}}$	$\frac{V_{PS}}{I_{QR}}$	$\frac{V_{SP}}{I_{RQ}}$	$\frac{R_{2a}+R_{2b}+R_{2c}+R_{2d}}{4}$
86.48 Ω	90.54 Ω	90.46 Ω	86.54 Ω	88.50 Ω

Similarly, the transresistance R_2 of the two-port network in Figure 6(b) is measured as the average of R_{2a} , R_{2b} , R_{2c} and R_{2d} , where values are tabulated in Table 3. All measurements in Tables 2 and 3 are carried out at $T = 300$ K without any applied field. The values of R_1 and R_2 are measured at different temperatures (at zero field) and the values of R_S are obtained thereby in the following section.

5.3 | Temperature sensitivity of R_1 , R_2 and R_S

The sample is maintained at different temperatures from 75 to 500 K in the cryogenic probe-station. At each temperature, for zero applied field, the values of R_1 and R_2 are measured for both the samples, following the procedure mentioned in Section 5.2.

The variation of R_1 with temperature is seen from Figure 8 (a). The measured values of R_2 vary with temperature, as shown in Figure 8(b), for the two samples. The measured values of R_1 and R_2 at each temperature are used to obtain the corresponding values of R_S using Equation (15). The variation of R_S with temperature is shown in Figure 8(c) for the two samples.

As seen from Figure 8(a–c), the values for the two samples are quite close, though there are minor variations, as should be expected, between the samples. The variations in R_1 , R_2 and R_S with temperature are all approximately parabolic. These resistances rise very significantly with temperature. The ratio of the transresistance at $T = 500$ K to that at $T = 75$ K is nearly 20. The same is valid for R_S as well.

The power dissipation of the Hall device is very small for the current bias used. At higher temperatures, where the sheet resistance is high, the power dissipation is limited to 20 μ W for both the samples. The temperature dependence of R_1 , R_2 or R_S can be used to determine the sample temperature, and thereby, to compensate for temperature variations in the current related sensitivity (or gain) of the Hall sensor.

6 | HALL SENSOR GAIN

The Hall sensor gain or the current related sensitivity is investigated experimentally under various conditions.

6.1 | Measurement of Hall voltage at a given temperature

For a given normal magnetic field, the bias current is injected into one terminal and drawn out of its diagonally opposite

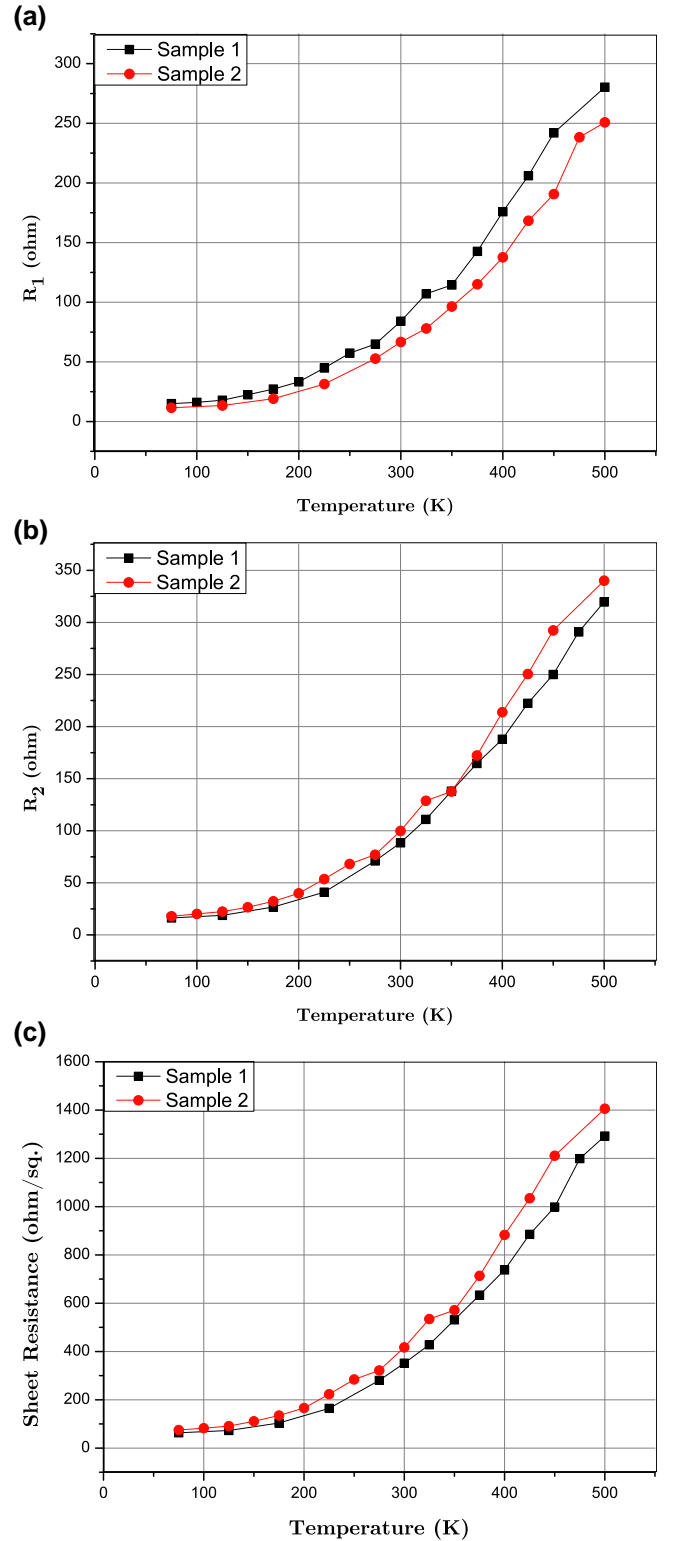


FIGURE 8 Measured variations in (a) transresistance R_1 , (b) transresistance R_2 , (c) sheet resistance R_S , with temperature

terminal; the Hall voltage is measured across the other pair of diagonal terminals. In the illustration in Figure 9, the bias current I_{PR} is injected into terminal P and taken out of R, and the Hall voltage is measured at terminal Q with respect to S.

The measured Hall voltage $V_{PR, QS}$ is 0.32 mV for $B = 0.25$ T and 3.86 mV for $B = -0.25$ T, as shown in Table 4. Thus, there is a large offset, which is inevitable due to multiple factors. Hence, current spinning is resorted to [72,73]. The Hall voltage $V_{RP, SQ}$ is measured at terminal S with respect to Q, reversing the bias current direction, for the same magnetic field strength. Hall measurements are also reported between terminals R and P, considering Q and S to be the current injection terminals. Thus, four different values of Hall voltage are measured for each magnetic field strength as indicated in Table 4. The average of these four values gives V_P for positive magnetic field; the same is designated as V_N if the magnetic

field is negative. It can be seen from Table 4 that the magnitudes of V_N and V_P are much closer for the same magnitude of magnetic flux density. Small differences in the magnitudes of V_N and V_P can be attributed to errors in the measurement of the Hall voltages and the magnetic field. In addition, the existence of residual offsets in the magnet can also contribute to such differences. The average of V_N and V_P is the Hall voltage V_H for the given magnetic field strength B . The V_H , thus obtained, is quite linear with the magnetic field B .

6.2 | Measurement of Hall voltages at different temperatures

The measurements in Table 4 are all carried out at $T = 300$ K. Similar measurements are carried out at different temperatures from 75 to 500 K in steps of 25 K. The measurements at 75, 125, 175, 225 and 275 K are plotted in Figure 10(a) for B ranging from 0.25 to 2.0 T. Similar measurements between 275 and 400 K are plotted in Figure 10(b). The Hall measurements at 400 and 500 K in Figure 10(c) are limited to a maximum B of 1 T (due to reasons mentioned earlier).

All the above measurements in Figure 10(a–c) are for sample 1. Similar measurements on sample 2 are presented in Figure 11(a–c). As seen from all the plots in Figures 10 and 11, the variation of V_H with B is fairly linear. This indicates that the non-linearities discussed in Section 2 are not too significant for these samples. Thus, the Hall coefficient, R_H , is reasonably independent of B . Hence, it is reasonable to use the idealised equations in Section 2.1 for evaluation of these Hall sensors.

6.3 | Current-related sensitivity

The current-related sensitivity (S_I) is obtained by dividing the measured Hall voltage by the product of the biasing current and applied normal field at each experimental condition as shown by (3). Figure 12(a) shows the temperature dependence of current related sensitivity for Sample 1 at three different normal fields. The obtained values of sensitivity for sample 1

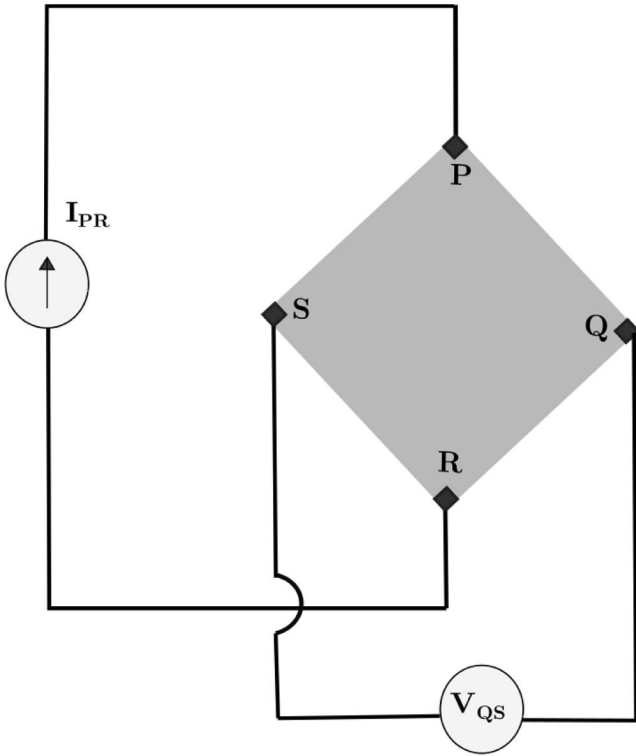


FIGURE 9 Schematic of Hall voltage measurement for the case $V_{BD, AC}$

TABLE 4 Hall voltages measured across different pairs of diagonal terminals by interchanging the voltage and current contacts at $T = 300$ K and $I = 100$ μ A

B (Tesla)	$V_{PR, QS}(mV)$		$V_{RP, SQ}(mV)$		$V_{SQ, PR}(mV)$		$V_{QS, RP}(mV)$		V_N (mV)	V_P (mV)	V_H (mV)
	–B	+B	–B	+B	–B	+B	–B	+B			
0.25	0.32	3.86	0.88	4.16	–4.16	–0.80	–3.86	–0.39	–1.70	1.71	1.71
0.50	–1.33	5.59	–0.85	5.92	–5.93	0.82	–5.64	1.34	–3.32	3.41	3.36
0.75	–2.94	7.29	–2.68	7.55	–7.68	2.56	–7.32	3.03	–5.15	5.10	5.13
1.00	–4.57	9.03	–4.46	9.19	–9.44	4.28	–9.05	4.80	–6.88	6.82	6.85
1.25	–6.36	10.83	–6.10	10.90	–11.40	6.01	–10.55	6.47	–8.60	8.55	8.58
1.50	–8.06	12.61	–7.83	12.59	–13.01	7.75	–12.42	8.19	–10.33	10.29	10.31
1.75	–9.86	14.26	–9.55	14.41	–14.66	9.63	–14.19	9.78	–12.06	12.02	12.04
2.00	–11.67	15.96	–11.26	16.13	–16.09	11.40	–16.26	11.58	–13.82	13.77	13.79

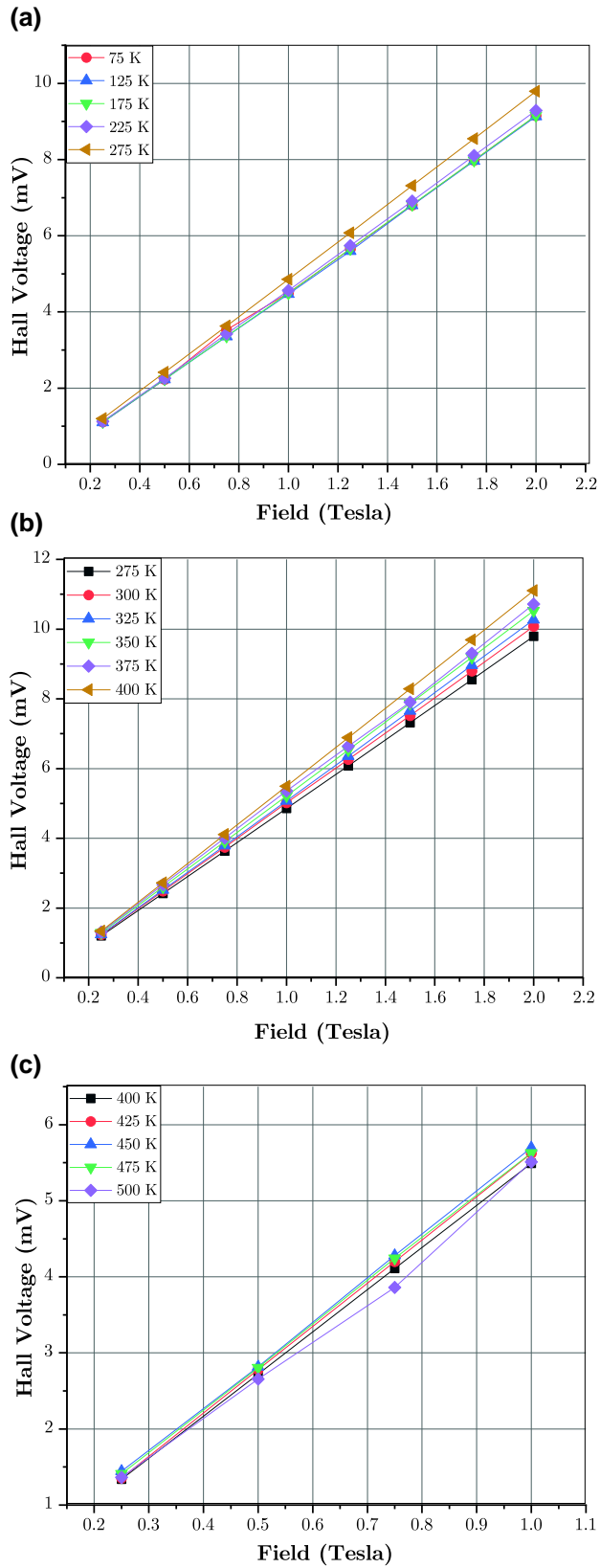


FIGURE 10 Hall voltage measured for sample 1 for different values of normal magnetic induction at temperatures from (a) 75 to 275 K, (b) 275 to 400 K and (c) 400 to 500 K

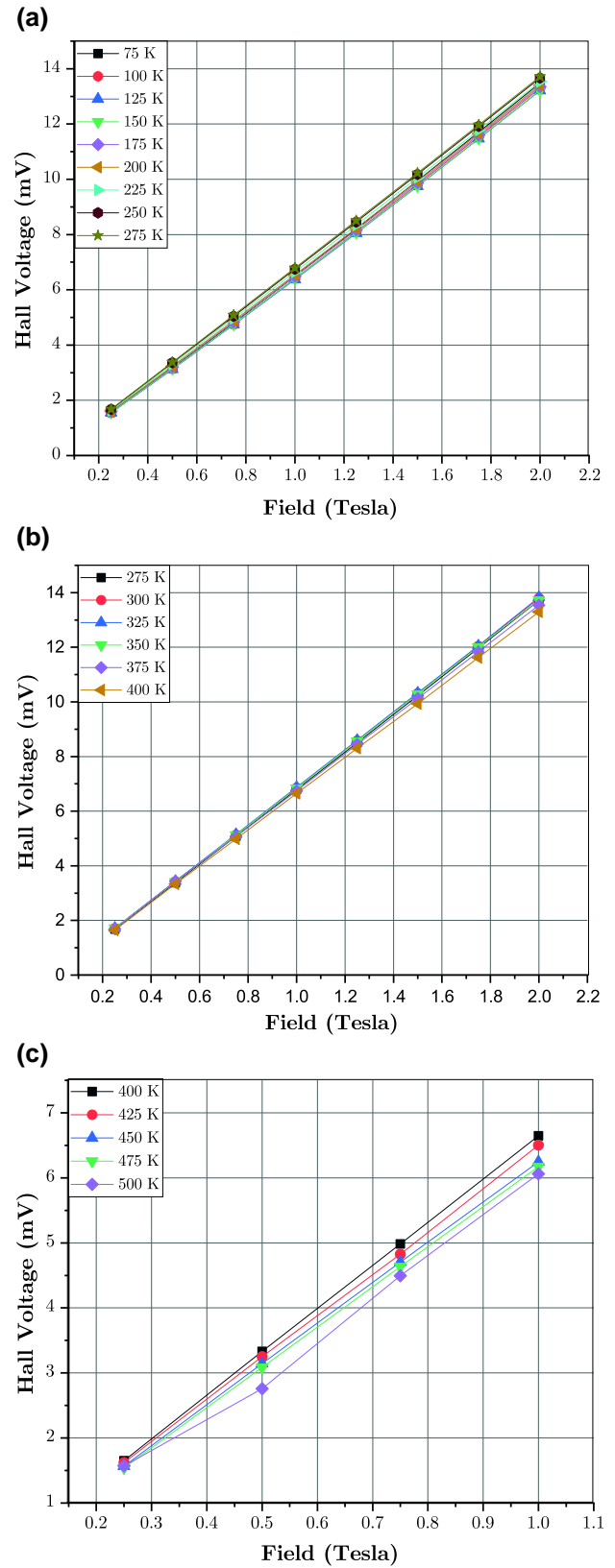


FIGURE 11 Hall voltage measured for sample 2 for different values of normal magnetic induction at temperatures from (a) 75 to 500 K, (b) 275 to 400 K and (c) 400 to 500 K

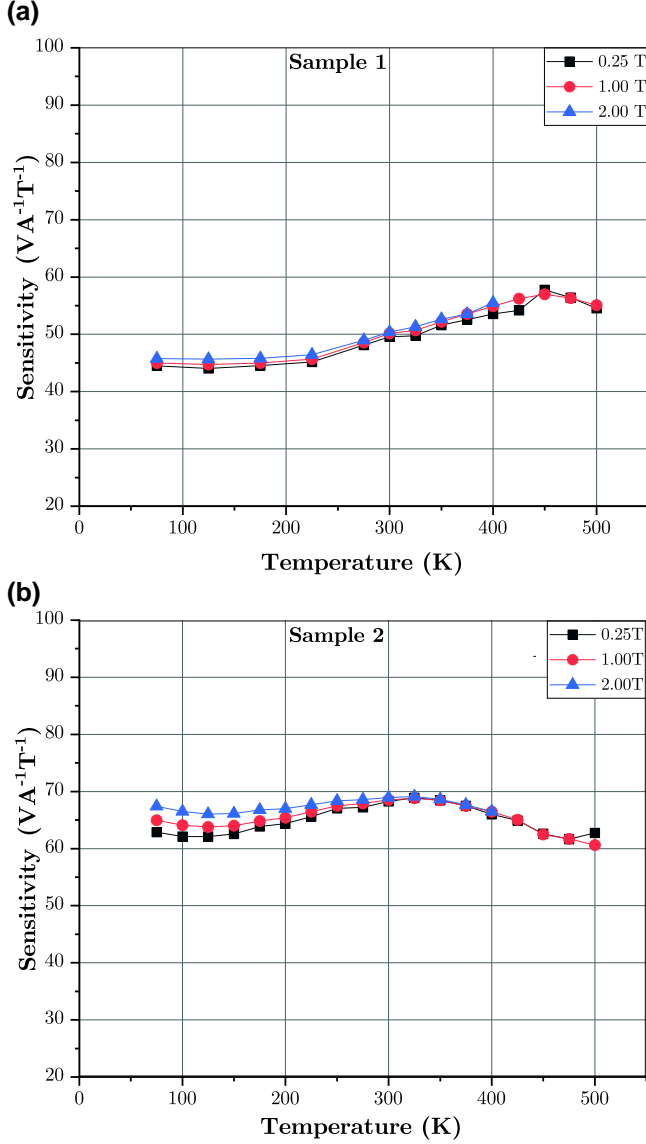


FIGURE 12 Current-related sensitivity based on measured Hall voltage at different applied magnetic field strengths and a constant current-bias of $100 \mu\text{A}$ for (a) sample 1 and (b) sample 2

fall in the range of $44\text{--}58 \text{ VA}^{-1}\text{T}^{-1}$. A similar plot for sample 2 is given by Figure 12(b). Sample 2 shows a slightly higher sensitivity than sample 1 at each operating point although they are diced from the same parent wafer. Here the obtained values of sensitivity fall in the range of $60\text{--}69 \text{ VA}^{-1}\text{T}^{-1}$.

The sensitivity plots confirm that 2DEG-based Hall sensors can have wider operating temperature range than a typical CMOS Hall sensing element where the working range is usually confined to the range 233 K to $+423 \text{ K}$ [37, 43, 44]. While existing literature on GaN-on-Si Hall sensors [51, 50] have reported Hall sensing up to 1 T , the present work establishes linear response over a much wider operating field magnitude of 2 T . From Figure 12, it can be concluded that the sensitivity of the hall element is fairly invariant with respect to temperature. Nevertheless, small variations in the Hall

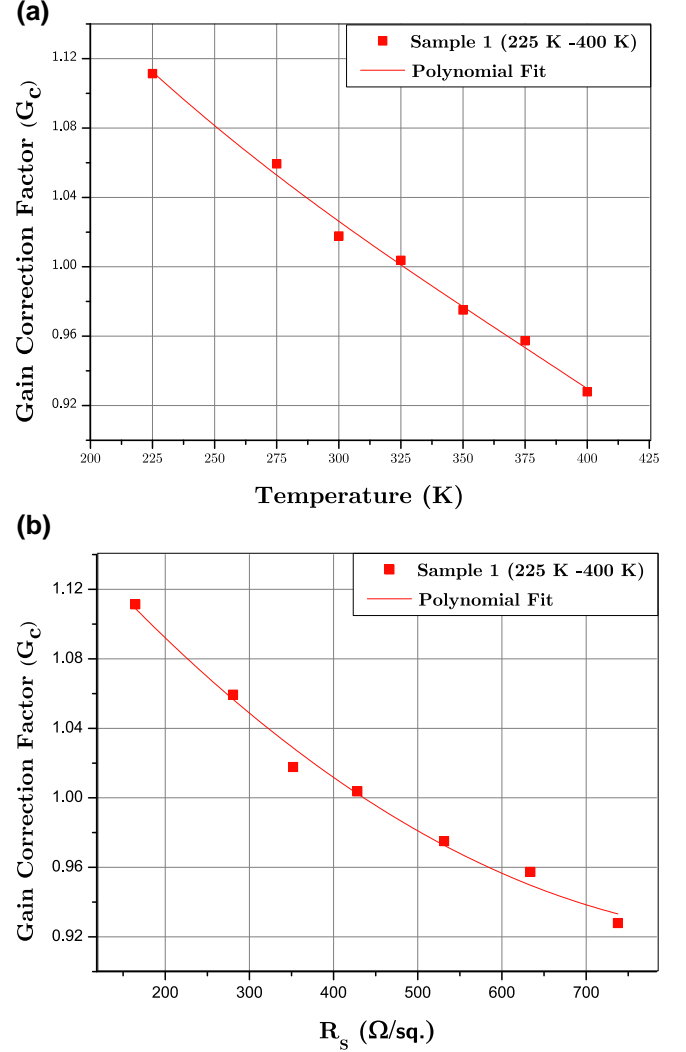


FIGURE 13 Variations in gain correction factor with (a) temperature from 225 up to 400 K and (b) transresistance R_s for sample 1 in the temperature range 225–400 K. A quadratic polynomial fit is also shown in the figure

element's sensitivity with temperature are unavoidable. This can be easily corrected by a gain correction factor (G_C) as discussed in the following section.

6.4 | Gain correction factor

Considering an application temperature range of 225 to 400 K, the average S_I can be obtained, which is designated as $S_{I,avg}$. The ratio of $S_{I,avg}$ to the actual temperature dependent $S_I(T)$ gives the required G_C as defined here:

$$G_C(T) = \frac{S_{I,avg}}{S_I(T)} \quad (16)$$

The G_C is a function of temperature as shown by Figure 13(a) and the sheet resistance R_s is a measure of temperature as discussed in Section 5.

One of the transresistances R_1 or R_2 can be a measure of temperature as discussed in Section 5. However, these transresistances can be shown to vary linearly with the applied normal induction B if the ohmic contacts are not exactly at the periphery of the sample [74]. The sheet resistance R_s , on the other hand, exhibits a much weaker dependence on B than the transresistance R_1 or R_2 [60]. Hence, G_C can be expressed as a function of sheet resistance R_s , as shown in Figure 13(b) which can be measured by the electronic subsystem of the Hall sensor. The measured sheet resistance R_s can then be used to choose the value of G_C to ensure uniform gain against temperature.

7 | EVALUATION OF GEOMETRICAL CORRECTION FACTOR

Based on the measurements in the previous section, the sheet carrier density and mobility of the two samples are evaluated at different values of B and T . These are then used to investigate the variations in G_H with respect to temperature and magnetic field. The Hall scattering factor r_b can potentially introduce additional complications in the calculation of the sheet carrier density and the carrier mobility. However, these errors are very small and are therefore neglected here.

7.1 | Estimated sheet carrier density

Sheet carrier density is estimated from current-related sensitivity using (3). Here r_b is assumed to be approximately equal to 1. The temperature dependence of sheet carrier density is plotted in Figure 14(a) and (b) for sample 1 and sample 2, respectively. Since, the sheet carrier density is inversely related to current-related sensitivity, there is a slight decrease in 2DEG concentration with temperature initially for both the samples. The sheet carrier density increases above 450 K for sample 1 and 350 K for sample 2. The variations in sheet carrier density are reasonably less for practical Hall sensing. This is in sharp contrast to the carrier density in Si. At high temperatures, the carrier density increases sharply due to intrinsic effects, thus degrading the sensitivity. Si-based Hall sensors therefore fail above 400 K [75].

7.2 | Estimated mobility

The measured sheet resistance (Figure 8) along with the estimated values of sheet carrier density yields mobility for each magnetic field and at each temperature using (5). r_b is approximated to unity as mentioned earlier. Similar to the sheet resistance, the mobility varies widely with temperature and decreases by a factor of 20 at 500 K compared to its value at 75 K (see Figure 15). The trend is in agreement with other surveys reported in literature on AlGaIn/GaN-based Hall sensors

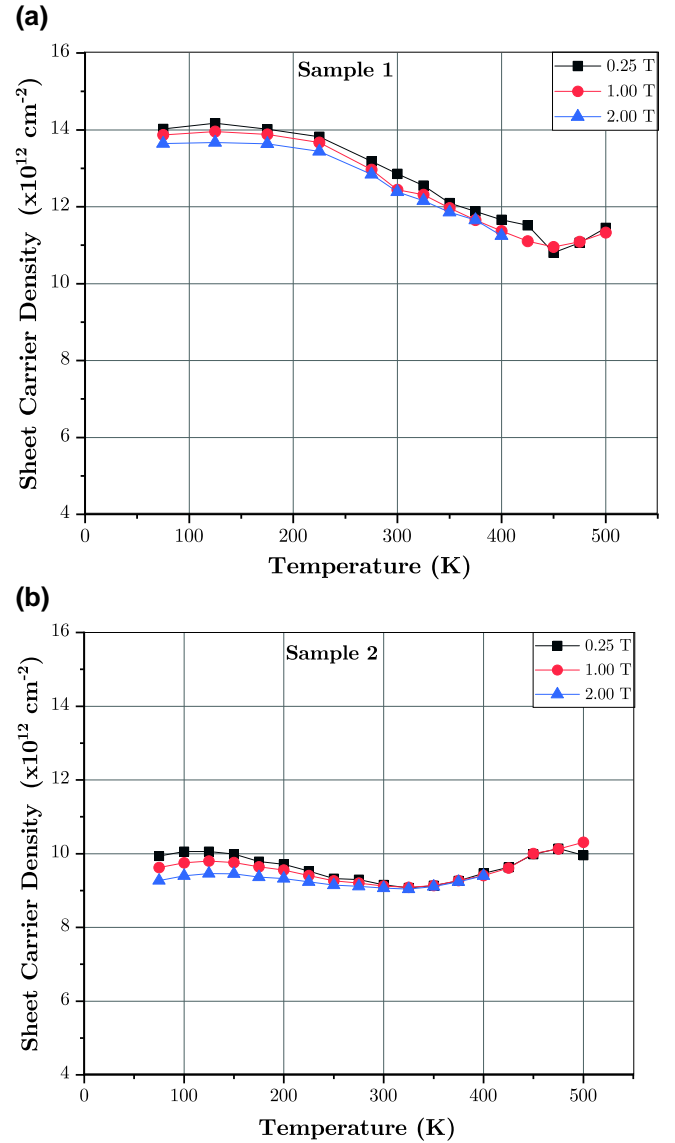


FIGURE 14 Sheet carrier density of 2DEG-based on the current-related sensitivity for (a) sample 1 and (b) sample 2 at different magnetic field strength

[32, 42, 48–50]. The estimated values of mobility are used to evaluate the geometrical correction factor.

7.3 | Geometrical correction factor

The geometrical factor is evaluated here using (13). At high values of B and very low temperature, μB is high. The geometrical correction factor can therefore be affected by large μB . However, the design of the sensor ensures that λ is practically very small. This ensures that the estimated geometrical correction factor is very high (around 0.97) and shows an increase of only 2% as the temperature is lowered to 75 K (Figure 16). Above room temperatures, it is estimated to remain fairly constant.

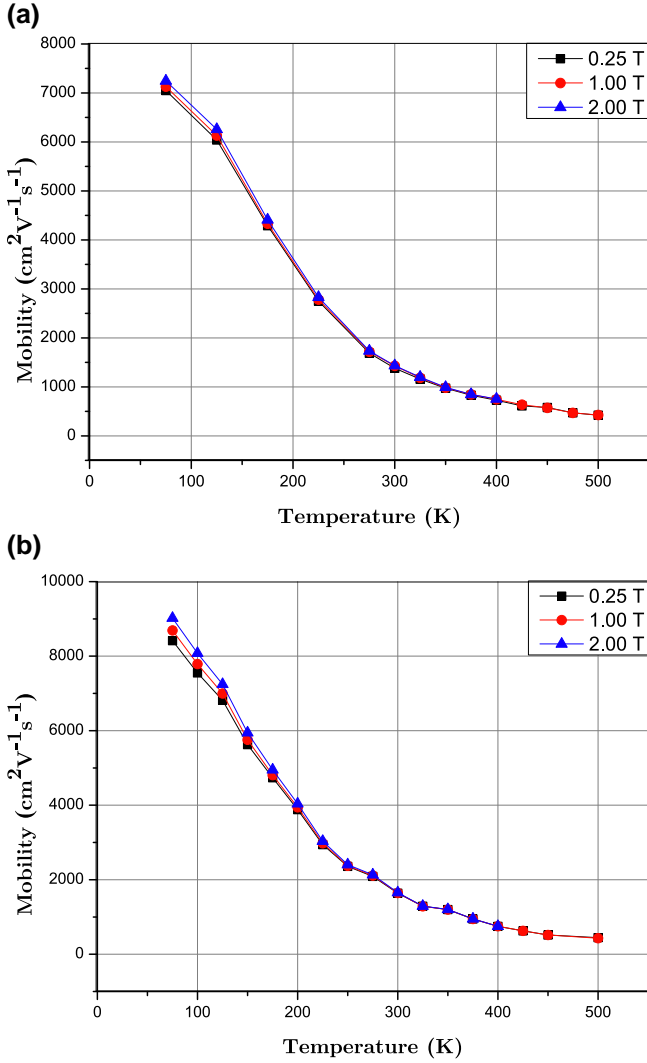


FIGURE 15 Mobility based on measured sheet resistance and estimated sheet carrier density for (a) sample 1 and (b) sample 2 at different values of magnetic field strength

8 | CONCLUSION

The authors discuss design, fabrication, characterisation and performance evaluation of Hall sensors based on AlGaIn/GaN heterojunctions grown on Si (111) substrates. The Hall sensors are characterised over a wide temperature range of 75–500 K, in steps of 25 K. Hall voltage is measured for normal magnetic fields in steps of 0.25 from -2 T to 2 T for temperatures up to 400 K and from -1 to 1 T for temperatures above 400 K. The obtained plots of the Hall voltage against B are observed to be fairly linear over the entire temperature range.

Experimental studies are conducted on the temperature dependence of the transresistances R_1 , R_2 and the sheet resistance R_s from 75 to 500 K. The temperature dependence of either the transresistance or the sheet resistance can be used to determine sample temperature. The current-related sensitivity of the Hall sensor is observed to be reasonably stable

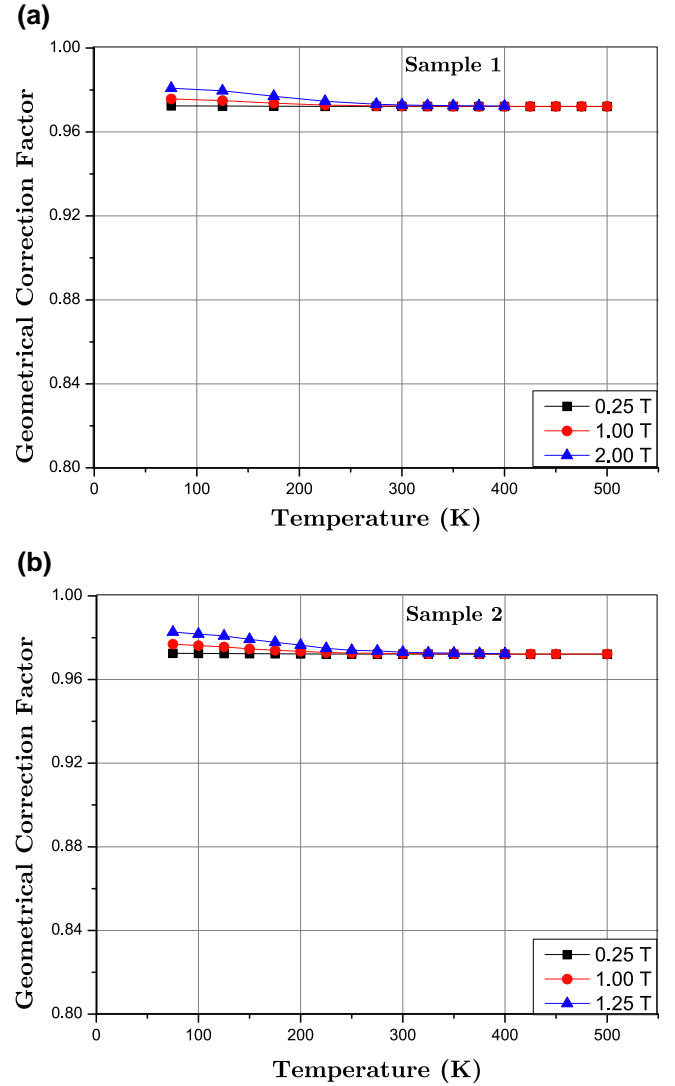


FIGURE 16 Estimated variations in geometrical correction factor with temperature for (a) sample 1 and (b) sample 2 at different magnetic field strength

over a wide temperature range of 75 to 500 K; minor variations are however observed. A method to compensate for the minor variations in sensitivity by employing the temperature dependence of the sheet resistance R_s or the transresistances R_1 and R_2 is proposed.

The mobility and sheet carrier density of the sample are estimated at each temperature. Despite variations in mobility with temperature, G_H is found to be fairly invariant ($<2\%$ variation) against temperature. This shows that even with a square geometry, which is known to be inferior to other geometries in terms of G_H , it is possible to achieve a high G_H that is also practically invariant with temperature and magnetic field.

Hall sensors based on AlGaIn/GaN heterostructures on Si substrates are a viable option for magnetic field measurement where the average flux density over a wide area needs to be measured as in the air gaps of electric machines. This technology lends itself to realisation of magnetic field measurement in different temperature ranges such as sub-zero or cryogenic

temperature range, commercial-grade temperature range, military-grade temperature range and high temperature range. This temperature range is much wider than the reported operating temperature ranges of Hall sensors based on Si, III–V thin films and quantum well AlGaAs/GaAs.

ACKNOWLEDGMENTS

The work of authors is supported by the Ministry of Electronics and Information Technology, Govt. of India, under a project titled: ‘High Performance Magnetic Field Sensors based on WBG Materials and High Bandwidth Current Sensors for WBG based Power Converters’ as part of the National Mission on Power Electronics Technology (NaMPET) Phase-III. The authors thank the staff and facility technologists of the National Nano Fabrication Facility (NNFC) and the Micro and Nano Characterisation Facility (MNCF) at the Centre for Nanoscience and Engineering, Indian Institute of Science, Bengaluru, for their technical support. The authors also acknowledge Dr. Sudhiranjan Tripathy of the Institute of Materials Research and Engineering (IMRE), Singapore for providing the wafers.

ORCID

Sagnik Kumar  <https://orcid.org/0000-0002-8413-3155>

REFERENCES

- Breiner, S.: Applications Manual for Portable Magnetometers. Geometrics, San Jose (1999)
- Diaz-Michelena, M.: Small magnetic sensors for space applications. *Sensors*. 9(4), 2271–2288 (2009)
- Whitehead, J.B., Grondahl, L.O.: Submarine detection in an alternating magnetic field. *J. Am. Inst. Electr. Eng.* 39(4), 381–395 (1920)
- Gao, J., et al.: Magnetic signature analysis for smart security system based on TMR magnetic sensor array. *IEEE Sensors J.* 19(8), 3149–3155 (2019)
- Filigrano, M.L., et al.: Triaxial fiber optic magnetic field sensor for magnetic resonance imaging. *J. Lightwave Technol.* 35(18), 3924–3933 (2017)
- Benndorf, C., Eckert, H., Janka, O.: Structural characterization of intermetallic compounds by ^{27}Al solid state NMR spectroscopy. *Acc. Chem. Res.* 50(6), 1459–1467 (2017)
- Okolo, C.K., Meydan, T.: Pulsed magnetic flux leakage method for hairline crack detection and characterization. *AIP Adv.* 8(4), 047207 (2018)
- Nakatani, T., Gao, Z., Hono, K.: Read sensor technology for ultrahigh density magnetic recording. *MRS Bull.* 43(2), 106–111 (2018)
- Chen, S.-C., Le, D.-K., Nguyen, V.-S.: Inductive displacement sensors with a notch filter for an active magnetic bearing system. *Sensors*. 14(7), 12640–12657 (2014)
- Song, X., Fang, J., Han, B.: High-precision rotor position detection for high-speed surface PMSM drive based on linear Hall-effect sensors. *IEEE Transactions on Power Electronics*. 31(7), 4720–4731 (2015)
- Li, Z., et al.: Study of current measurement method based on circular magnetic field sensing array. *Sensors*. 18(5), 1439 (2018)
- Lei, C., et al.: Measurement of inrush current in transformer based on optical current transducer. *J. Phy. Conf. Series*. IOP Publishing. 1187(2), 022004 (2019)
- Merazzo, K., et al.: Reading magnetic ink patterns with magnetoresistive sensors. *AIP Adv.* 8(5), 056633 (2018)
- Tangelder, R.J., Diemel, G., Kerkhoff, H.G.: Smart sensor system application: an integrated compass. *Proc. Eur. Design Test Conf. ED & TC*, 97, 195–199. *IEEE* (1997)
- Kapsalis, V.: Advances in magnetic field sensors *J. Phys. Conf. Series*, 939, 012026 (2017)
- Lenz, J.E.: A review of magnetic sensors. *Proc. IEEE*. 78(6), 973–989 (1990)
- Mosser, V., Matringe, N., Haddab, Y.: A spinning current circuit for Hall measurements down to the nanotesla range. *IEEE Trans. Instrum. Meas.* 66(4), 637–650 (2017)
- Borges, J.C.S., et al.: New contactless torque sensor based on the Hall effect. *IEEE Sensors J.* 17(16), 5060–5067, Filho (2017)
- Zidat, F., et al.: Non-invasive sensors for monitoring the efficiency of AC electrical rotating machines. *Sensors*. 10(8), 7874–7895 (2010)
- Jung, S.-Y., Nam, K.: PMSM control based on edge-field hall sensor signals through ANF-PLL processing. *IEEE Trans. Ind. Electron.* 58(11), 5121–5129 (2011)
- Shaw, G., et al.: A scanning Hall probe microscope for high resolution, large area, variable height magnetic field imaging. *Rev. Sci. Instrum.* 87(11), 113702 (2016)
- Passeri, D., et al.: Magnetic force microscopy: quantitative issues in biomaterials. *Biomatter*. 4(1), e29507 (2014)
- Okeil, H., Wachutka, G.: A perspective on magnetic field sensors operating under extreme high-temperature conditions. *IEEE Trans. Magnet.* 55(1), 1–4 (2018)
- Primadani, Z., Osawa, H., Sandhu, A.: High temperature scanning Hall probe microscopy using AlGaIn/GaN two dimensional electron gas micro-Hall probes. *J. Appl. Phys.* 101(9), 09K105 (2007)
- Yamamura, T., et al.: High sensitivity and quantitative magnetic field measurements at 600 °C. *J. Appl. Phys.* 99(8), 08B302 (2006)
- Bolshakova, I., et al.: Prospects of using In-containing semiconductor materials in magnetic field sensors for thermonuclear reactor magnetic diagnostics. *IEEE Trans. Magnet.* 49(1), 50–53 (2012)
- Patel, A., Ferdowsi, M.: Current sensing for automotive electronics—a survey. *IEEE Trans. Veh. Technol.* 58(8), 4108–4119 (2009)
- Boles, T.: GaN-on-silicon—present capabilities and future directions *AIP Conf. Proc.* 1934. 020001 (2018)
- Hassan, A., Savaria, Y., Sawan, M.: GaN integration technology, an ideal candidate for high-temperature applications: a review. *IEEE Access*, 6(6), 78790–78802 (2018)
- Li, Y., et al.: Stress and dislocation control of GaN epitaxial films grown on Si substrates and their application in high-performance light-emitting diodes. *J. Alloys Compound*. 771, 1000–1008 (2019)
- Alpert, H.S., et al.: Effect of geometry on sensitivity and offset of AlGaIn/GaN and InAlIn/GaN Hall-effect sensors. *IEEE Sensors J.* 19(10), 3640–3646 (2019)
- White, T.P., et al.: AlGaIn/GaN micro-Hall effect devices for simultaneous current and temperature measurements from line currents. *IEEE Sensors J.* 18(7), 2944–2951 (2018)
- Safonov, D.A., et al.: Electron Transport in PHEMT AlGaAs/InGaAs/GaAs Quantum Wells at Different Temperatures: Influence of One-Side δ -Si Doping. *Semiconductors*. 52(2), 189–194 (2018)
- Nakamura, T., Maenaka, K.: Integrated magnetic sensors. *Sensor. Actuator. A Phys.* 22(1-3), 762–769 (1990)
- Oszwaldowski, M.: Hall sensors based on heavily doped n-InSb thin films. *Sensor. Actuator. A Phys.* 68(1-3), 234–237 (1998)
- Iwabuchi, T., et al.: High sensitivity Hall elements made from Si-doped InAs on GaAs substrates by molecular beam epitaxy. *J. Cryst. Growth*. 150, 1302–1306 (1995)
- Putley, E.H., Mitchell, W.H.: The electrical conductivity and Hall effect of silicon. *Proc. Phys. Soc.* 72(2), 193 (1958)
- Kuze, N., Shibusaki, I.: MBE research and production of hall sensors. *III-Vs Rev.* 10(1), 28–32 (1997)
- Mosser, V., et al.: High sensitivity Hall sensors with low thermal drift using AlGaAs/InGaAs/GaAs heterostructures. *Sensors Actuators A: Physical*. 43(1-3), 135–140 (1994)
- Alpert, H.S., et al.: Sensitivity of 2DEG-based Hall-effect sensors at high temperatures. *Rev. Sci. Instrument.* 91(2), 025003 (2020)
- Bando, M., et al.: High sensitivity and multifunctional micro-Hall sensors fabricated using InAlSb/InAsSb/InAlSb heterostructures. *Journal of Applied Physics*. 105, 07E909 (2009)

42. Koide, S., et al.: High temperature Hall sensors using AlGaIn/GaN HEMT structures. *J. Phys. Conf. Ser.* 352(1), 012009 (2012)
43. DRV5053 Analog-Bipolar Hall Effect Sensor. <http://www.ti.com/lit/ds/symlink/drv5053.pdf>. Accessed 12 October 2019
44. 2D, Dual-Channel, Ultrasensitive Hall-Effect Latch. <https://www.allegromicro.com/en/Products/Sense/Switches-and-Latches/Dual-Hall-Effect-Latches/A1262.aspx>. Accessed 22 March 2021
45. HW-108A: InSb Hall Element. <https://www.akm.com/eu/en/products/magnetic-sensor/hall-element/in-sb-ultra-high-sensitivity/hw108a/>. Accessed 22 March 2021
46. CYTY Series (InSb) Hall-effect elements. <http://www.hallsensors.de/CYTY-InSb.pdf>. Accessed 22 March 2021
47. Hall sensors: SH Series. <https://buy.fwbell.com/hall-effect-sensors/sh-400.html>. Accessed 22 March 2021
48. Abderrahmane, A., et al.: Robust Hall effect magnetic field sensors for operation at high temperatures and in harsh radiation environments. *IEEE Trans. Magn.* 48(11), 4421–4423 (2012)
49. Lu, H., et al.: High temperature Hall effect sensors based on AlGaIn/GaN heterojunctions. *J. Appl. Phys.* 99(11), 114510 (2006)
50. Bouguen, L., et al.: Investigation of AlGaIn/AlIn/GaN heterostructures for magnetic sensor application from liquid helium temperature to 300° C. *Appl. Phys. Lett.* 92(4), 043504 (2008)
51. Consejo, C., et al.: High temperature electrical investigations of (Al,Ga)N/GaN heterostructures - Hall sensor applications. *phys. stat. sol. (c)* 2(4), 1438–1443 (2005)
52. AHS: P2A Hall Sensor. <https://www.ahsLtd.com/p2a-hall-sensor>. Accessed 22 March 2021
53. EQ-431L Hybrid liner Hall effect ICs. <https://www.ahsLtd.com/p2a-hall-sensor>. Accessed 22 March 2021
54. Gaska, R., et al.: Self-heating in high-power AlGaIn-GaN HFETs. *IEEE Electron Device Lett.* 19(3), 89–91 (1998)
55. Sheppard, S.T., et al.: High-power microwave GaN/AlGaIn HEMTs on semi-insulating silicon carbide substrates. *IEEE Electron Device Lett.* 20(4), 161–163 (1999)
56. Liu, L., Edgar, J.H.: Substrates for gallium nitride epitaxy. *Mater. Sci. Eng. R Report.* 37(3), 61–127 (2002)
57. Ryou, J., Lee, W.: GaN on sapphire substrates for visible light-emitting diodes. In: Huang, J., Kuo, H., Shen, S. (eds.) *Nitride Semiconductor Light-Emitting Diodes (LEDs): Materials, Technologies and Applications* (Woodhead Publishing Series in Electronic and Optical Materials, 2nd edn., pp. 43–67. Elsevier, Duxford (2018)
58. Kazior, T.E., et al.: High performance mixed signal and RF circuits enabled by the direct monolithic heterogeneous integration of GaN HEMTs and Si CMOS on a silicon substrate. In: 2011 IEEE Compound Semiconductor Integrated Circuit Symposium, pp. 1–4. (CSICS), Waikoloa, HI (Oct. 2011)
59. Kazior, T.E.: Beyond CMOS: heterogeneous integration of III–V devices, RF MEMS and other dissimilar materials/devices with Si CMOS to create intelligent microsystems. *Philosoph. Trans. Royal Soc. A Math. Phys. Eng. Sc.* 372(2012), 20130105 (2014)
60. Popović, R.: Hall-effect devices. *Sensor. Actuator.* 17(1-2), 39–53 (1989)
61. Versnel, W.: Analysis of symmetrical Hall plates with finite contacts. *J. Appl. Phys.* 52(7), 4659–4666 (1981)
62. Ausserlechner, U.: The signal-to-noise ratio and a hidden symmetry of Hall plates. *Solid-State Electron.* 135, 14–23 (2017)
63. Automatic Dicing Saw DAD322. <https://www.disco.co.jp/eg/products/catalog/pdf/dad322.pdf>. Accessed 22 March 2021
64. Manual Mask Aligner SUSS MJB4: Versatile System For R & D Applications and Low-Volume Production. <https://www.suss.com/brochures-datashets/mask-aligner-mjb4.pdf>. Accessed 22 March 2021
65. E-Beam Evaporator (TECPORT) Manual, Training Document, National Nano Fabrication Centre, Indian Institute of Science, Bangalore, 2015
66. Campbell, S.A.: Physical deposition: evaporation and sputtering. In: Adel S. Sedra (ed.) *The Science and Engineering of Microelectronic Fabrication*, 2nd edn., pp. 295. Oxford University Press, New York (2001)
67. AS-One RTP System. <https://www.annealsys.com/products/annealsys-products/rtp-and-rtcvd/as-one.html>. Accessed 22 March 2021
68. User's Manual CRX-VF Probe Station: Lake Shore Cryotronics. Westerville, Ohio rev.1.0 (2012)
69. Qing, F., et al.: A general and simple method for evaluating the electrical transport performance of graphene by the van der Pauw-Hall measurement. *Sci. Bull.* 63(22), 1521–1526 (2018)
70. van Der PAUW, L.J.: A method of measuring specific resistivity and Hall effect of discs of arbitrary shape. *Philips. Res. Rep.* 13(1), 1–9 (1958)
71. Ausserlechner, U.: Closed form expressions for sheet resistance and mobility from Van-der-Pauw measurement on 90° symmetric devices with four arbitrary contacts. *Solid-State Electron.* 116(116), 46–55 (2016)
72. Munter, P.J.A.: A low-offset spinning-current Hall plate. *Sensors Actuators A Phys.* 22(1-3), 743–746 (1990)
73. Steiner, R., et al.: Offset reduction in Hall devices by continuous spinning current method. *Sensors Actuator. A Phys.* (66)(1-3), 137–172 (1998)
74. Marion, D., Cristoloveanu, S., Chovet, A.: High-magnetic-field Van der Pauw method Magnetoresistance measurement and applications. *IEE Proc. I Solid State Electron. Devices UK.* 129(4), 125–130 (1982)
75. Manic, D., Petr, J., Popovic, R.: Temperature cross-sensitivity of Hall plate in submicron CMOS technology. *Sensor. Actuator. A Phys.* (851-3), 244–248 (2000)

How to cite this article: Kumar S, Muralidharan R, Narayanan G. Hall-effect sensors based on AlGaIn/GaN heterojunctions on Si substrates for a wide temperature range. *IET Circuits Devices Syst.* 2021;1–15. <https://doi.org/10.1049/cds2.12067>